

The shape of dark matter haloes: results from weak lensing in the Ultraviolet Near-Infrared Optical Northern Survey (UNIONS)

Bailey Robison^{1,2*}, Michael J. Hudson^{1,2,3}, Jean-Charles Cuillandre⁴, Thomas Erben⁵, Sébastien Fabbro⁶, Raphaël Gavazzi^{7,8}, Axel Guinot^{9,10}, Stephen Gwyn¹¹, Hendrik Hildebrandt¹², Martin Kilbinger^{9,13}, Alan McConnachie⁶, Lance Miller¹⁴, Isaac Spitzer^{1,2}, Ludovic van Waerbeke¹⁵

¹*Department of Physics and Astronomy, University of Waterloo, Waterloo, ON, N2L 3G1, Canada*

²*Waterloo Centre for Astrophysics, Waterloo, ON, N2L 3G1, Canada*

³*Perimeter Institute for Theoretical Physics, 31 Caroline St. N., Waterloo, ON, N2L 2Y5, Canada*

⁴*AIM, CEA, CNRS, Université Paris-Saclay, Université de Paris, F-91191, Gif-sur-Yvette, France*

⁵*Argelander-Institut für Astronomie, Auf dem Hügel 71, 53121 Bonn / Germany*

⁶*NRC Herzberg Astronomy & Astrophysics, 5071 West Saanich Road, British Columbia, Canada V9E2E7*

⁷*Sorbonne Université, CNRS, UMR7095, Institut d'Astrophysique de Paris, F-75014, Paris, France*

⁸*Institute of Astronomy, University of Cambridge, Madingley Road, Cambridge CB30HA, UK*

⁹*AIM, CEA, CNRS, Université Paris-Saclay, Université de Paris, 91191 Gif-sur-Yvette, France*

¹⁰*Université de Paris, CNRS, Astroparticule et Cosmologie, F-75013 Paris, France*

¹¹*Canadian Astronomy Data Centre, Herzberg Astronomy and Astrophysics, National Research Council, 5071 West Saanich Rd, Victoria BC, V9E 2E7*

¹²*Ruhr-Universität Bochum, Astronomisches Institut, German Centre for Cosmological Lensing (GCCL), Universitätsstr. 150, 44801, Bochum, Germany*

¹³*Institut d'Astrophysique de Paris, UMR7095 CNRS, Université Pierre & Marie Curie, 98 bis boulevard Arago, 75014 Paris, France*

¹⁴*Department of Physics, University of Oxford, Denys Wilkinson Building, Keble Road, Oxford OX1 3RH, UK*

¹⁵*Department of Physics and Astronomy, University of British Columbia, 6224 Agricultural road, Vancouver, BC V6T 1Z1, Canada*

Accepted XXX. Received YYY; in original form ZZZ

ABSTRACT

Cold dark matter haloes are expected to be triaxial, and so appear elliptical in projection. We use weak gravitational lensing from the Canada-France Imaging Survey (CFIS) component of the Ultraviolet-Near Infrared Optical Northern Survey (UNIONS) to measure the ellipticity of the dark matter haloes around Luminous Red Galaxies (LRGs) from the Sloan Digital Sky Survey Data Release 7 (DR7) and from the CMASS and LOWZ samples of the Baryon Oscillation Spectroscopic Survey (BOSS), assuming their major axes are aligned with the stellar light. We find that DR7 LRGs with masses $M \sim 2.5 \times 10^{13} M_{\odot}/h$ have halo ellipticities $e = 0.35 \pm 0.09$. Expressed as a fraction of the galaxy ellipticity, we find $f_h = 1.4 \pm 0.4$. For BOSS LRGs, the detection is of marginal significance: $e = 0.17 \pm 0.10$ and $f_h = 0.1 \pm 0.4$. These results are in agreement with other measurements of halo ellipticity from weak lensing and, taken together with previous results, suggest an increase of halo ellipticity of 0.10 ± 0.05 per decade in halo mass. This trend agrees with the predictions from hydrodynamical simulations, which find that at higher halo masses, not only do dark matter haloes become more elliptical, but that the misalignment between major axis of the stellar light in the central galaxy and that of the dark matter decreases.

Key words: gravitational lensing: weak – galaxies: haloes – cosmology: dark matter

1 INTRODUCTION

In the standard Λ CDM cosmological model of our universe, dark matter accounts for over 80% of the matter content and plays a dominant role in the formation and evolution of large scale structure in the universe. Dark matter haloes, in which galaxies reside, assemble in a hierarchical manner, with less massive haloes accreting onto more massive ones. Simulations have revealed that filaments and other forms of large scale structure will have an effect on the rate and direction of the accretion of smaller haloes (Van Haarlem & van

de Weygaert 1993), and that this leads to triaxial dark matter haloes that appear elliptical in projection (Dubinski & Carlberg 1991; Jing & Suto 2002; Bailin & Steinmetz 2005), with more massive haloes tending to be more elliptical (Allgood et al. 2006).

This halo anisotropy has implications for cosmological studies with weak lensing. Weak lensing operates under the assumption that galaxies are randomly oriented, while in reality they will have alignments due to gravity of surrounding structure. Therefore, this intrinsic alignment is a significant source of contamination. Improving our model of halo anisotropy will allow us to develop a better understanding of these intrinsic alignments, which will improve the results of future weak lensing studies. Dark matter halo anisotropy

* E-mail: baileyarobison@gmail.com

also provides a test to rule out theories of modified gravity (Milgrom 2013; Khoury 2015), and provides a method to constrain the cross section of self-interacting dark matter (Davé et al. 2001; Peter et al. 2013).

The distribution of satellite galaxies has been used to infer the shape of dark matter haloes. Studies have focused on the distribution of satellite galaxies with respect to the shape of the central galaxy (Brainerd 2005; Azzaro et al. 2007). A preferential alignment of the satellite distribution with the major axis of the light of the central galaxy is evidence of a non-spherical dark matter distribution. This preferential alignment has been confirmed by observations (Yang et al. 2006) and in simulations (Zentner et al. 2005; Libeskind et al. 2007).

Weak lensing is another method of detecting dark matter halo anisotropy (Natarajan & Refregier 2000; Brainerd & Wright 2000). This involves measuring the azimuthal dependence of the shear. Natarajan & Refregier (2000) proposed splitting the weak lensing shear into monopole and quadrupole terms, where the quadrupole is aligned with major axis of the galaxy’s light. Hoekstra et al. (2004) introduced the measurement of f_h , the ratio of the aligned ellipticities of haloes and galaxy light, and measurements of f_h have been made by Mandelbaum et al. (2006a) and Schrabback et al. (2015). Recently, this method has been used by Schrabback et al. (2021) to obtain a 3.8σ detection of halo ellipticity, one of the most significant detections of anisotropy of galaxy-scale haloes. Brainerd & Wright (2000) proposed comparing the weak lensing signal within 45 deg of the major and minor axes, a method implemented by Parker et al. (2007). This method was also utilised by Van Uitert et al. (2017) to obtain a significant detection of halo ellipticity in group-scale haloes. The method was extended and improved by Clampitt & Jain (2016) who found a 4σ detection of the halo ellipticity of luminous red galaxies (LRGs) from the Sloan Digital Sky Survey (SDSS). This method has been used to measure the halo ellipticity of massive galaxy cluster haloes (Evans & Bridle 2009; Oguri et al. 2010), where the lensing is much stronger.

In this paper, we present a new measurement of halo ellipticity from weak lensing. In Section 2, we present the source and lens data used in this paper. In Section 3 we explain our methods of analysis, including the anisotropic halo model and the various estimators used to measure quadrupole shear. We present our results in Section 4. These include results from the monopole shear and the average halo ellipticity from the quadrupole shear. A discussion of systematic effects is given in Section 5. Section 6 includes a comparison with previous results. Finally, in Section 7 we present our conclusions and prospects for future results.

The adopted cosmology is a flat Universe with $\Omega_m = 0.3$ and we quote all factors that depend on H_0 using $h \equiv H_0/(100 \text{ km/s/Mpc})$. There are two conventions for galaxy (or halo) “ellipticity”, and in this paper, for comparison with the literature, we will need to use both. We adopt the following notation: $e \equiv \frac{a^2-b^2}{a^2+b^2}$ and $\epsilon \equiv \frac{a-b}{a+b}$, where a and b are the major and minor axes, respectively.

2 DATA

2.1 Source galaxies from UNIONS

The sources used in our weak lensing analysis were derived from the r -band component of the Ultraviolet Near-Infrared Optical Northern Survey (UNIONS)¹. UNIONS is a deep wide-field multi-band

(*ugriz*) imaging survey covering the high Galactic latitude sky north of 30 degrees declination (approximately 4,800 square degrees). The r -band component of UNIONS was obtained at the Canada-France-Hawaii Telescope as part of the Canada-France Imaging Survey (CFIS, Ibata et al. 2017) with a median seeing of 0.68 arcseconds and a $10\text{-}\sigma$ limiting magnitude of 24.1 for extended sources in the r -band.

The UNIONS r -band data used in this paper cover 1,565 square degrees of the northern hemisphere, containing roughly 46 million source galaxies. This coverage can be divided into 4 contiguous regions, referred to as “patches”. To save computer time and memory, the weak lensing analysis is performed on each of these individual patches rather than on the entire source catalogue simultaneously. The patches are large enough that any effects from being near the edge of the source catalogue are minimal. Patch 1 is the largest, containing nearly half of the sources. Patch 4 contains roughly a quarter of the sources, while Patches 2 and 3 contain roughly an eighth.

Galaxy shape measurements, necessary for weak lensing, are generated using an early version of SHAPEPIPE, a new shape measurement pipeline (Guinot et al. 2022). The pipeline uses the ngmix package (Sheldon 2015) to perform METACALIBRATION (Huff & Mandelbaum 2017) which yields the ellipticities ϵ_1 and ϵ_2 for each source. Each source is assigned a statistical weight that quantifies how well the image is fit by the resulting shape. The weight is given by

$$w = \frac{1}{2\sigma_{\text{int}}^2 + \sigma_{\epsilon_1}^2 + \sigma_{\epsilon_2}^2} \quad (1)$$

The intrinsic shape noise is $\sigma_{\text{int}} = 0.34$ for both components (Guinot et al.). The two parameters $\sigma_{\epsilon_i}^2$ are the variances of measurement errors on the ellipticities.

To convert the shear into a mass distribution, we need the critical surface mass density

$$\Sigma_{\text{crit}} = \frac{c^2}{4\pi G} \frac{D_s(z_s)}{D_l(z_l)D_{ls}(z_l, z_s)}, \quad (2)$$

where the distances are angular diameter distances that depend on the lens or source redshifts, or both. At present, UNIONS data do not have complete deep *ugriz* photometry, and photometric redshifts of the source galaxies are not yet available. Nevertheless we can make a statistical determination of the critical density if the source redshift distribution is known. We have measured $p(z_s)$ using the method described in Lima et al. (2008), with the implementation of Hildebrandt et al. (2017, 2020). Full details of the application of this method to UNIONS are given in Spitzer et al. (submitted); here we give a brief summary. We match the UNIONS catalogue with the W3 patch of the deeper Canada-France-Hawaii Lensing Survey (CFHTLenS), which overlaps with UNIONS to obtain *ugriz* photometry for CFIS sources. Then, a spectroscopic sample, with *ugriz* photometry from CFHTLenS, was used (Hildebrandt et al. 2012; Erben et al. 2013), and galaxies in this sample were reweighted until their distribution in 5-dimensional colour space matched that of the *ugriz* UNIONS catalogue. The resulting reweighted $p(z)$ from the sample was then adopted as the $p(z)$ for the UNIONS catalogue. The resulting $p(z)$ is fit by the profile described in equation (3). We also create versions of the catalogue that are magnitude limited and fit with the same profile to account for varying depth across the field. The distribution of parameters as a function of weighted median r -band magnitude is fit by equations (4) and (5). We fit the data with a

¹ <https://www.skysurvey.cc/>

source redshift function of

$$p(z) = \left(A(m) \cdot \frac{z^\alpha \cdot e^{-\left(\frac{z}{z_0(m)}\right)^\alpha}}{z_0^{\alpha+1} \cdot \Gamma\left(\frac{\alpha+1}{\alpha}\right)} \right) + \left((1 - A(m)) \cdot \frac{e^{-\frac{(z-\mu)^2}{2\sigma^2}}}{2.5046} \right), \quad (3)$$

$$A(m) = -0.4154m^2 + 19.1734m - 220.261, \quad (4)$$

$$z_0(m) = 0.1081m - 1.9417, \quad (5)$$

where $\alpha = 1.79$, $\sigma = 1.3$, $\mu = 1$ and where m is the median weighted r -band magnitude. This median r -band magnitude is different for each of the 4 patches, so each patch will use a slightly different $p(z)$ and $\Sigma_{\text{crit}}^{-1}(z_1)$. The median magnitude for Patch 1 is $m = 22.95$, for Patch 2 it is $m = 22.944$, for Patch 3 it is $m = 22.923$, and for Patch 4 it is $m = 22.952$. The process of fitting $p(z)$ was undertaken by Spitzer et al. (submitted).

We then calculate the average *inverse* critical density, following Viola et al. (2015), by integrating over the probability density function of the source galaxy redshifts as follows

$$\langle \Sigma_{\text{crit}}^{-1}(z_1) \rangle = \frac{4\pi G}{c^2} \int_{z_1}^{\infty} \frac{D_1(z_1) D_{1s}(z_1, z_s)}{D_s(z_s)} p(z_s) dz_s. \quad (6)$$

This can be evaluated for each lens and incorporated into the weighted average to obtain the excess surface mass density (ESD), $\Delta\Sigma$.

We note, however, that the halo ellipticity is robust to the source redshift distribution because it depends on a ratio of the quadrupole moment of the ESD to the monopole of the ESD. Therefore, any systematic error in the ESD, due to, for example, a systematic error in the source redshift distribution, will appear in both numerator and denominator, and hence will cancel.

2.2 Lens Galaxies

Luminous Red Galaxies (LRGs) are used as lenses because they reside in massive dark matter haloes, with a typical halo mass on the order of $10^{13} - 10^{14} h^{-1} M_\odot$ (Zheng et al. 2009a). A more massive halo has a stronger weak lensing signal, which makes it easier to detect the quadrupole component of the shear. Also, simulations suggest that more massive haloes also tend to be more elliptical (Allgood et al. 2006). Finally, LRGs provide a reliable method of aligning our lensing measurements. The distribution of satellite galaxies, which may trace the dark matter halo, are more aligned with the galaxy light for red central galaxies (Yang et al. 2006).

We consider two LRG samples in this paper. One lens sample consists of LRGs from the SDSS DR7 catalogue of Kazin et al. (2010). These LRGs span a redshift range of $0.15 < z < 0.5$ with a median redshift $z = 0.34$ and a median lens galaxy ellipticity of $e = 0.22$. Only LRGs that overlap with the current UNIONS weak lensing footprint were used, resulting in a lens sample of approximately 18,000 LRGs.

The second lens sample consists of the LRGs from the CMASS and LOWZ samples of the BOSS component of SDSS-III (Dawson et al. 2013). These LRGs are selected within several magnitude and colour criteria, and span a redshift range of $0.15 < z < 0.7$. Only LRGs that overlap with the current UNIONS footprint were used. This resulted in a lens sample of approximately 144,000 lenses with a median redshift of $z = 0.51$ and a median lens galaxy ellipticity of $e = 0.22$.

In order to measure the anisotropy of the shear signal, the lenses need to be aligned before stacking. We first matched the SDSS LRG

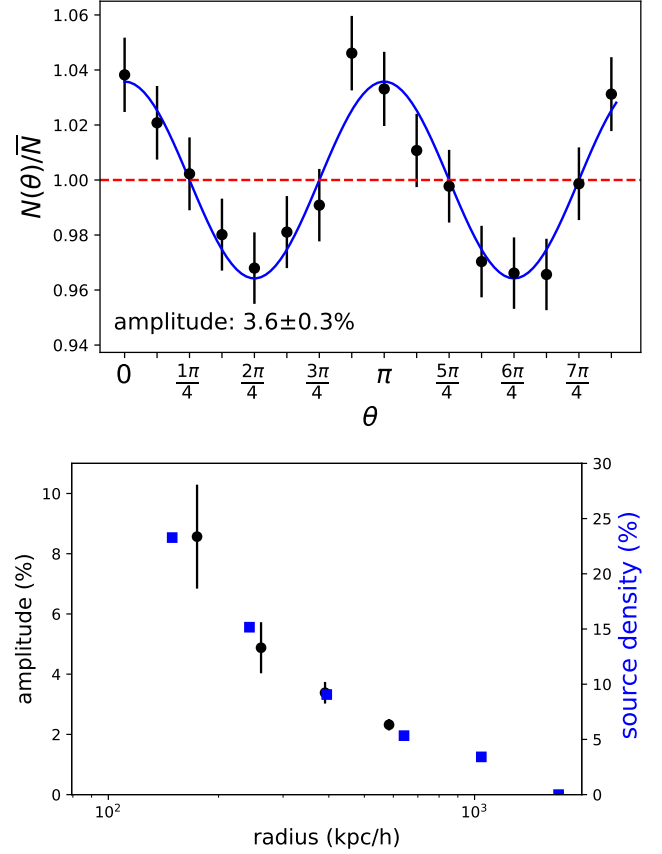


Figure 1. Top: Weighted source galaxy counts in 16 azimuthal bins as a function of angle from the major axis of the LRG’s stellar light. Only source galaxies with a projected separation of 140-700 kpc/h are included. A function of the form $\cos(2\theta)$ was fit with the amplitude as a free parameter. The vertical axis is scaled to show deviation from the mean. Bottom: Amplitude fit to azimuthal source distribution as a function of radius (black circles). The right-hand scale and the blue squares show the excess counts above background.

catalogue with UNIONS photometric catalogues on position. Many LRGs are too large or bright for our standard shape measurement pipelines, which are designed for small faint galaxies near the survey limit. Instead, the shape and orientation of LRG in UNIONS was obtained from the position angles and axis ratios in the UNIONS r -band SExtractor (Bertin & Arnouts 1996) catalogue. The SExtractor position angles are not corrected for PSF anisotropy, but the source galaxy shapes are. So in principle, there should be no correlation between shapes of lenses and sources. Nevertheless, as a test, we also perform the analysis with LRG position angles derived from independent SDSS photometry in Section 5.

Later, we will discuss how the results might be affected by the possible contamination by satellite galaxies of our source sample. Due to the lack of photometric redshifts for the sources, there is no way to determine if a given source is actually behind the lens. Thus it is possible that some of the sources around the lens are actually satellite galaxies. If this is the case, we expect there to be an excess of sources along the major axis of the lens light and a deficit along the minor axis. In this section, we will discuss the azimuthal distribution of sources around the lenses.

The lenses were rotated to a coordinate system where the major axis of the lens galaxy light (as measured in the UNIONS catalogue) is aligned with the x -axis. The weighted source galaxy counts within an

annulus 140-700 kpc/h around each LRG were binned by azimuthal angle from the major axis. For each angular bin, the uncertainty is the square root of the number of sources in the bin. Results for the DR7 LRGs are displayed in the upper panel Fig. 1. The azimuthal distribution of sources has a quadrupole dependence, with more sources along the major axis and fewer along the minor axis. Fitting a function of the form $\cos(2\theta)$, we find amplitude of the source galaxy azimuthal distribution function from the fit is $(3.6 \pm 0.3)\%$.

We have investigated whether this anisotropy depends on radius. To quantify the radial dependence, we fit $\cos(2\theta)$ for all angular bins for a given radial bin. Results are shown in the lower panel of Fig. 1. We find that the amplitude of the $\cos(2\theta)$ dependence varies with radius. This dependence is quite strong at a distance of 170 kpc/h from the lens, but decreases as distance from the centre increases. This is a reflection of the fraction of satellites compared to all background sources, as shown on the right-hand axis, and suggests that the satellite population has an approximately constant ellipticity.

For the BOSS LRGs, the amplitude of the source galaxy azimuthal distribution function from the fit is $1.5 \pm 0.3\%$, which is lower than that found for DR7 LRGs. This may arise because the BOSS LRGs are at greater distances than the DR7 LRGs, and hence the satellites have lower contrast with the background, or because the BOSS LRGs are somewhat less massive, or possibly because the BOSS LRGs are slightly less aligned with their haloes than the original set of LRGs.

It is interesting to compare these results with previous work. Yang et al. (2006) studied several groups from SDSS. They divided the area around the central galaxies into angular bins and calculated the normalised pair count for each angular bin $f_{\text{pairs}}(\theta) = N(\theta)/\langle N_R(\theta) \rangle$, where $N_R(\theta)$ are counts where the central galaxy major axis angle has been randomised. In the angular bin along the major axis, $f_{\text{pairs}} \sim 1.2$, which can also be thought of as a $\sim 20\%$ quadrupole dependence in order to compare with our quadrupole amplitude. Most of our sources are not satellites, and it is not possible to separate the background sources from genuine satellites. As a result our amplitude is much smaller. We also observe a radial dependence, with the amplitude decreasing as radius increases and the possibility of finding satellites becoming increasingly unlikely.

If satellites trace the halo, this suggests that the dark matter halo is well aligned with the lens light. Therefore, we will use the lens light as a proxy for the major axis of the halo when stacking to measure the quadrupole shear. In addition to their usefulness as a possible proxy for shape of the dark matter haloes, satellite galaxies are also a potential source of contamination for our shear measurements. Satellite galaxy orientations are expected to be preferentially aligned with the central galaxy (Schneider & Bridle 2010; Georgiou et al. 2019), which could lead to a radial bias in the shear. The role of satellites as a potential systematic effect will be discussed further in Section 6.

3 ANALYSIS

Before measuring the halo ellipticity, we first determine the mass and concentration of the LRG halo. This is done by measuring the monopole component of the tangential shear. This is commonly calculated as a weighted average of the source galaxy ellipticities. All sources have a weight, w , that describes the quality of the source's shape measurement. We also weight each lens-source pair by $W_1 = \langle \Sigma_{\text{crit}}^{-1}(z_1) \rangle^2$ following Sheldon et al. (2004), with $\langle \Sigma_{\text{crit}}^{-1}(z_1) \rangle$ from equation (6). The excess mass density is given by

$$\langle \Delta\Sigma(R) \rangle = \frac{\sum \epsilon_{t,s} \langle \Sigma_{\text{crit}}^{-1}(z_1) \rangle w_s W_1}{\sum w_s W_1}, \quad (7)$$

summing over all sources, s , and all lenses, l , with a given radial separation.

After measuring the monopole shear, we measure the quadrupole shear. This process is different, as we need to take the orientation of the lenses into account. First, the positions of the lens and the sources are converted from equatorial coordinates into a local 2D Cartesian coordinate system centred on the lens. All data, including the positions and shapes of the sources, are rotated so that the major axis of the light in the lens is aligned with the x -axis of the coordinate system. This process is repeated for each lens to measure the azimuthal variation in the shear and stack the results.

3.1 Model

We need a model in order to relate the measured shear to the mass and ellipticity of the dark matter halo. The model consists of a 1-halo term ($\Delta\Sigma_{1h}$) which describes the matter associated with the lens galaxy. Normally, we would also include an offset group term to account for lenses that reside within subhaloes inside a larger host halo. However, few of the LRGs are expected to be satellite galaxies: for example, from halo occupation modelling, Zheng et al. (2009b) predict satellite fractions of 2-5% (depending on luminosity) for DR7 LRGs. The satellite fraction for the BOSS LRGs, which are less massive than the DR7 LRGs, is somewhat higher but still low: about 10% (White et al. 2011; Parejko et al. 2013). Consequently we neglect this term in the modelling. A 2-halo term is often included to account for the lensing signal from neighbouring haloes. This term is important at large radii, but not within the radial range we are concerned with in this work.

The 1-halo term is comprised of the contribution from the stellar mass of the galaxy and the mass of the galaxy's dark matter halo. The stellar mass is treated as a point mass,

$$\Delta\Sigma_*(R) = M_*/\pi R^2. \quad (8)$$

We also require a term to describe the dark matter halo in the 1-halo term. Normally, an NFW profile is used to describe the density profile of a dark matter halo. However, the mass of the NFW profile does not converge when integrated to an infinite radius. Instead, we use a truncated NFW profile from Baltz et al. (2009) to describe the dark matter halo, which has a well defined total mass. The truncated NFW profile is

$$\rho(x) = \frac{M_0}{4\pi r_s^3} \frac{1}{x(1+x)^2} \frac{\tau^2}{\tau^2 + x^2}, \quad (9)$$

where $x = r/r_s$ and $M_0 = 4\pi\rho_s r_s^3$. The truncation factor, $\tau = r_t/r_s$, describes the radius where the truncation term begins to dominate. For the remainder of this paper, a truncation factor of $\tau = 10$ is used. The scale radius of the halo, r_s , is related to the virial radius (R_{200}) through the concentration (c_{200c}). The virial radius is the radius in which the average density is 200 times the critical density of the universe (ρ_c). This is related to the virial mass as follows:

$$M_{200c} = \frac{4\pi}{3} R_{200c}^3 (200\rho_c). \quad (10)$$

So if we know c_{200c} and M_{200c} we can calculate the scale radius

$$r_s = R_{200c}/c_{200c} = \left(\frac{3}{4\pi} \frac{1}{200\rho_c} M_{200c} \right)^{1/3} / c_{200c}. \quad (11)$$

The scale density, ρ_s , is related to the critical density and also depends on the concentration.

$$\rho_s = \frac{200}{3} \frac{c_{200c}^3}{\ln(1+c_{200c}) - \frac{c_{200c}}{1+c_{200c}}} \rho_c \quad (12)$$

We parametrise the NFW profile using only M_{200c} and c_{200c} . For an NFW profile with a given M_{200c} and c_{200c} , we can find r_s using equation (11) and ρ_s using equation (12).

The projected surface mass density for the truncated NFW profile ($\Delta\Sigma_{\text{NFW}}$) is derived in Baltz et al. (2009). The total one-halo term is comprised of this truncated NFW profile and the stellar mass term from equation (8).

$$\Delta\Sigma_{1h} = \Delta\Sigma_* + \Delta\Sigma_{\text{NFW}} \quad (13)$$

Now we can extend this model to account for the halo ellipticity. The surface mass density of the anisotropic halo can be split into a monopole, described by a projection of the truncated NFW profile, and a quadrupole term:

$$\Sigma(R, \theta) = \Sigma_0(R) \left[1 - \frac{e}{2} \eta_0(R) \cos(2\theta) \right], \quad (14)$$

where θ is defined as the angle measured counter-clockwise from the major axis of the mass distribution. The ellipticity of the halo is represented by e . The function $\eta_0(R)$ describes how the quadrupole term is related to the monopole term at different radii. Clampitt & Jain (2016) use

$$\eta_0(R) = \frac{d \log \Sigma_0(R)}{d \log R} = \frac{R}{\Sigma_0(R)} \frac{d \Sigma_0(R)}{d R}, \quad (15)$$

which is based on a model developed by Adhikari et al. (2015).

3.2 Halo ellipticity Estimators

Here we consider two different estimators of the halo ellipticity that differ in how the ellipticity is measured. The purpose of these estimators is to measure the quadrupole signal, which is proportional to the halo ellipticity, while cancelling any contribution from the monopole shear.

The first of the quadrupole estimators used in this paper are from Clampitt & Jain (2016), and will be referred to as the CJ estimators. These estimators measure the halo ellipticity directly, independently of the ellipticity of the galaxy. Moreover, they nullify the purely tangential monopole lensing signal. They provide 4 statistically independent measurements of halo ellipticity that we will combine to calculate the mean halo ellipticity. A potential bias in the halo ellipticity arises if some effect aligns the major axis of the BCG in the same sense as the background sources. This might occur due to cosmic shear if foreground large-scale structure that is closer than the BCG, shears both the BCG and the background sources in the same sense. Alternatively, an uncorrected PSF anisotropy may also affect both the BCG and the background sources. However, this systematic only affects the $\Delta\Sigma_1^{(+/-)}$ estimators and not the $\Delta\Sigma_2^{(+/-)}$ estimators (Clampitt & Jain 2016).

The second set of estimators assume that the halo ellipticity is related to the ellipticity of the lens galaxy stellar light, e_g . These estimators were first introduced by Hoekstra et al. (2004), further developed by Mandelbaum et al. (2006a), and will be referred to here as Hoekstra-Mandelbaum (HM) estimators. The $f\Delta\Sigma$ and $f_{45}\Delta\Sigma$ estimators will both be affected by a systematic shear, as described above. However, to a good approximation, the two estimators will both be equally affected by this spurious shear (Mandelbaum et al. 2006a), and therefore, by subtraction, we can measure the uncontaminated value $(f - f_{45})\Delta\Sigma$. Schrabback et al. (2015) tested this with ray-tracing simulations and showed that the cancellation of systematics works well, at least for lenses at low redshift and for lens-source pairs at low projected galactocentric radii (see their fig. 6). These estimators are used to calculate the aligned ellipticity ratio $f_h \sim e_h/e_g$.

Because the two sets of halo ellipticity estimators weight and combine the source shapes in different ways, they are statistically correlated, but not perfectly (nor of course are they statistically independent). We will consider both estimators in this paper.

3.2.1 Clampitt-Jain Estimators

A given source will have shape measurements (ϵ_1, ϵ_2) after rotation to align with the major axis of the light. Each of these shape components will have a corresponding mass density. These mass densities will make use of the two functions $I_1(R)$ and $I_2(R)$.

$$I_1(R) = \frac{3}{R^4} \int_0^R R'^3 \Sigma_0(R') \eta_0(R') dR' \quad (16)$$

$$I_2(R) = \int_R^\infty \frac{\Sigma_0(R') \eta_0(R')}{R'} dR' \quad (17)$$

The estimators will make use of the shape measurements and Σ_{crit} . Adhikari et al. (2015) give these as

$$\Sigma_{\text{crit}} \gamma_1(R, \theta) = (e/4) [(2I_1(R) - \Sigma_0(R) \eta_0(R)) \cos 4\theta + 2I_2(R) - \Sigma_0(R) \eta(R)] \quad (18)$$

$$\Sigma_{\text{crit}} \gamma_2(R, \theta) = (e/4) [2I_1(R) - \Sigma_0(R) \eta_0(R)] \sin 4\theta \quad (19)$$

We will be using 4 estimators. The first pair of estimators, $\Delta\Sigma_1^{(+)}$ and $\Delta\Sigma_1^{(-)}$, use the γ_1 shape measurement. The estimators will be either + or - depending on the sign of $\cos(4\theta)$, which appears in equation (18).

$$\Delta\Sigma_1^{(+)}(R) = \frac{4}{\pi} \int_{-\pi/8}^{\pi/8} \Sigma_{\text{crit}} \gamma_1(R, \theta) d\theta + 3 \text{ rotations by } \pi/2 \quad (20)$$

$$\Delta\Sigma_1^{(-)}(R) = \frac{4}{\pi} \int_{\pi/8}^{3\pi/8} \Sigma_{\text{crit}} \gamma_1(R, \theta) d\theta + 3 \text{ rotations by } \pi/2 \quad (21)$$

where each of bounds have 3 additional $\pi/2$ rotations so that they cover a + or X shape on the sky. The final pair of estimators, $\Delta\Sigma_2^{(+)}$ and $\Delta\Sigma_2^{(-)}$, will use the γ_2 shape measurement. The sign of these estimators will depend on the sign of $\sin(4\theta)$ which appears in equation (19).

$$\Delta\Sigma_2^{(+)}(R) = \frac{4}{\pi} \int_0^{\pi/4} \Sigma_{\text{crit}} \gamma_2(R, \theta) d\theta + 3 \text{ rotations by } \pi/2 \quad (22)$$

$$\Delta\Sigma_2^{(-)}(R) = \frac{4}{\pi} \int_{\pi/4}^{\pi/2} \Sigma_{\text{crit}} \gamma_2(R, \theta) d\theta + 3 \text{ rotations by } \pi/2 \quad (23)$$

In practice, we measure these from the data with a weighted average of the source ellipticities

$$\Delta\Sigma_k^{(s)} = \frac{\sum w_s \epsilon_{k,s} \Sigma_{\text{crit},l} W_1}{\sum w_s W_1}, \quad (24)$$

where $k = 1, 2$ refers to which ellipticity component (γ_k) is used in the weighted average. The angular range of the weighted average changes depending on k and s .

$$\begin{aligned} k = 1, s = + : & \quad -\pi/8 \leq \theta < \pi/8 \\ k = 1, s = - : & \quad \pi/8 \leq \theta < 3\pi/8 \\ k = 2, s = + : & \quad 0 \leq \theta < \pi/4 \\ k = 2, s = - : & \quad \pi/4 \leq \theta < \pi/2 \end{aligned} \quad (25)$$

with each of these having 3 other $\pi/2$ rotations so that they cover a + or × shape on the sky.

To obtain the halo ellipticity, we compare the model predictions from equations (20) – (23) to the measurements from equation (24) and fit for the unknown parameter, e .

3.2.2 Hoekstra-Mandelbaum Estimators

The HM estimators assume that the halo ellipticity depends on the lens galaxy stellar ellipticity, e_g as follows:

$$\Delta\Sigma(r) = \Delta\Sigma_{\text{iso}}(r) [1 + 2f(r)e_g \cos(2\theta)] . \quad (26)$$

Note that this differs by a factor of 2 from the model used by [Schraback et al. \(2015\)](#), who adopt a different definition of lens galaxy ellipticity. This yields two estimators, $f\Delta\Sigma$ and $f_{45}\Delta\Sigma$, that depend on the tangential and cross shear components (ϵ_t and ϵ_\times).

$$f(r)\Delta\Sigma(r) = \frac{\sum_i w_i \Sigma_{\text{crit}}^{-1} e_{g,i} \epsilon_{t,i} \cos(2\theta_i)}{2 \sum_i w_i \Sigma_{\text{crit}}^{-2} e_{g,i}^2 \cos^2(2\theta_i)} , \quad (27)$$

$$f_{45}(r)\Delta\Sigma(r) = \frac{\sum_i w_i \Sigma_{\text{crit}}^{-1} e_{g,i} \epsilon_{\times,i} \sin(2\theta_i)}{2 \sum_i w_i \Sigma_{\text{crit}}^{-2} e_{g,i}^2 \sin^2(2\theta_i)} , \quad (28)$$

where

$$\epsilon_t = -\epsilon_1 \cos 2\theta - \epsilon_2 \sin 2\theta , \quad (29)$$

$$\epsilon_\times = +\epsilon_1 \sin 2\theta - \epsilon_2 \cos 2\theta . \quad (30)$$

It is worth noting that the sign convention for the shears are different than for the CJ estimators. For example, a source at an angle of $\theta = 0$ experiencing a purely vertical shear would have a negative ϵ_1 ellipticity component. However, this would be a positive tangential shear, or a positive ϵ_t ellipticity component.

The HM estimators are useful when calculating the aligned ellipticity ratio, $f_h \sim e_h/e_g$. This ratio describes the weighted average ratio of the aligned projected ellipticity of the dark matter haloes and their embedded galaxies. The following method was described by [Mandelbaum et al. \(2006a\)](#) and [Schraback et al. \(2015\)](#). The two estimators receive equal contributions from systematic effects. Therefore, $(f - f_{45})\Delta\Sigma_{\text{iso}}(r)$ provides a systematic-free measure of halo ellipticity. The relative asymmetry in the shear field is described by the functions $f_{\text{rel}}(r)$ and $f_{\text{rel},45}(r)$. They are related to $f(r)$ and $f_{45}(r)$ through a factor of f_h . These depend on the density profile of the halo and need to be computed numerically. We obtained discrete values for $f_{\text{rel}}(r)$ and $f_{\text{rel},45}(r)$ from [Mandelbaum et al. \(2006a\)](#). They were computed for NFW profiles in terms of the scale radius, r_s , of the NFW profile. We use the average scale radius for our lens sample and interpolate on these values.

Now that we have $f_{\text{rel}}(r)$ and $f_{\text{rel},45}(r)$, we define

$$\widehat{y}(r) = \frac{1}{f_{\text{rel}}(r) - f_{\text{rel},45}(r)} (f - \widehat{f_{45}})\Delta\Sigma_{\text{iso}}(r) , \quad (31)$$

$$\widehat{x}(r) = \widehat{\Delta\Sigma_{\text{iso}}}(r) . \quad (32)$$

These are two random variables with a Gaussian distribution. Each point in the monopole density profile corresponds to a measurement of $\widehat{x}(r)$, while the HM estimators correspond to measurements of $\widehat{y}(r)$. At each point, we calculate

$$\widehat{f}_h(r) = \frac{\widehat{y}(r)}{\widehat{x}(r)} . \quad (33)$$

To obtain the value of f_h , we take a weighted mean of each of these measurements within the mean virial radius of the haloes of our lens sample. The weights are proportional to the standard deviation in the measurements, $w = \sigma_{f_h,i}^{-2}$.

3.2.3 Misalignment between the position angles of the stellar light and the dark matter halo

We expect the light of the LRGs to be aligned with their dark matter haloes, making the major axis of the light a proxy for the major axis of the dark matter halo. The alignment, however, is not perfect and has been studied by a number of authors.

If the probability density function of misalignment angles is $P(\theta_{\text{mis}})$, then the aligned ellipticity e_{eff} will be reduced from the halo ellipticity by a factor ([Clampitt & Jain 2016](#))

$$\frac{e_{\text{eff}}}{e} = \langle \cos(2\theta_{\text{mis}}) \rangle = \int \cos(2\theta_{\text{mis}}) P(\theta_{\text{mis}}) d\theta_{\text{mis}} . \quad (34)$$

For example, if one assumes $P(\theta_{\text{mis}})$ is a Gaussian distribution with width σ_{mis} in radians, then

$$\frac{e_{\text{eff}}}{e} = \exp(-2\sigma_{\text{mis}}^2) \quad (35)$$

One way to assess the degree of misalignment is through hydrodynamical simulations of galaxy formation that predict the distribution of misalignment angles, $P(\theta_{\text{mis}})$. A number of authors have studied the misalignment angle between the projected stellar distribution and the projected total matter distribution in various halo mass bins. They find the misalignment angle tends to be smaller in more massive haloes. In Appendix A, we compute relevant quantities for the case of [Velliscig et al. \(2015\)](#). We return to the topic of misalignment in the discussion in Section 6.

4 RESULTS

4.1 Weak Lensing Monopole Results

Before fitting the elliptical model to the quadrupole shear, we require the monopole of the shear. The monopole of the tangential shear was measured in radial bins and scaled using Σ_{crit} for each lens galaxy. Then an NFW profile was fit with halo mass and concentration as free parameters. Only bins within 1 Mpc/h from the centre of the lens were included in the fit, as beyond this radius effects from other haloes and surrounding structures become significant. A sample of 10,000,000 random lenses was created, and the lensing signal around these random lenses was measured. Before fitting, we subtract the results of the random lenses from the measured signal.

The results of the stacking and the fit for the DR7 LRGs are shown in Fig. 2. Both parameters are quite well constrained, and there is good agreement between the data within 1 Mpc/h and the NFW model. We obtain a halo mass of $M_{200c} = (2.47 \pm 0.13) \times 10^{13} M_\odot/h$ and a concentration of $c_{200c} = 2.99 \pm 0.30$.

The mass is consistent with that found by [Mandelbaum et al. \(2006b\)](#), for which a lens-weighted average over their bright and faint DR4 LRG subsamples yields $(3.04 \pm 0.39) \times 10^{13} M_\odot/h$, after conversion to our mass definition. Similarly converted, their concentration is 2.8 ± 0.4 , which is in good agreement with our result.

The concentration from the fit is lower than the concentration predicted by mass-concentration relations. For a halo of this mass, [Duffy et al. \(2008\)](#) predict a concentration $c_{200c} \sim 4$, while [Dutton & Macciò \(2014\)](#) predict $c_{200c} \sim 5$. Our model consists of only a 1-halo term. In reality, some of the LRGs will be satellites inside of

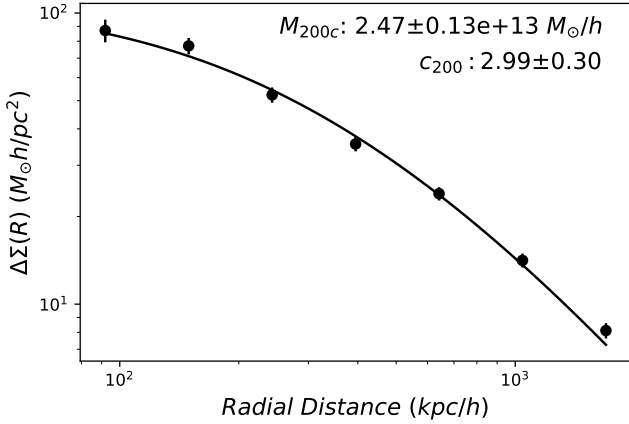


Figure 2. The monopole tangential shear of the DR7 LRGs with the best fitting NFW halo fit using bins within 1 Mpc/h. The best-fitting halo mass and concentration are displayed in the plot.

a larger halo. This is normally described by the inclusion of an offset group term. Neighbouring haloes will also contribute to the lensing signal, which can be described by a 2-halo term. These terms are not included in the model, so it is not meaningful to compare to standard mass-concentration relations. If we were to include these terms, we would measure a different mass and concentration. Regardless, the model fits the data well, which is all that is necessary in order to extract the ellipticity.

For the BOSS LRGs, we obtain a halo mass of $M_{200c} = (1.08 \pm 0.03) \times 10^{13} M_{\odot}/h$ and a concentration of $c_{200c} = 1.97 \pm 0.13$.

4.2 Weak Lensing Quadrupole

Results for the CJ estimators applied to the DR7 LRGs are displayed in Fig. 3. An elliptical model was fit to each of the 4 quadrupole estimators separately. This model used the halo mass and concentration from the monopole fit, with only e as a free parameter. Only radial bins within 600 kpc/h were included in the fit, as surrounding structure contributes a significant amount of anisotropy at large radius. The region not included in the fit is shaded in gray. The best fit of e for each CJ estimator is displayed in the appropriate panel.

We can quantify the significance of the agreement between these ellipticity values from the fits. A weighted average of the halo ellipticity is taken using the uncertainty in the value of e from the fit ($w = \sigma_e^{-2}$). The 4 ellipticities from the CJ estimators are independent of each other, because they cover different angular ranges around the lens and different components of the ellipticity. From the 4 CJ estimators, the mean halo ellipticity is $e = 0.347 \pm 0.091$. If we assume these 4 values of ellipticity are fit with a constant, we can calculate the χ^2 of this hypothetical fit with the mean e as the constant. The value of $\chi^2 = 5.67$. Evaluating the cumulative distribution function for a χ^2 with 3 degrees of freedom yields a probability of 13% that $\chi^2 \geq 5.67$, so the fit is acceptable. We show the constant model and the data in Fig. 3. When these estimators are fit with an ellipticity of $e = 0$, the value raises to $\chi^2 = 20.24$, with a probability of 0.02%.

Results for the HM estimators are displayed in Fig. 4. For the DR7 LRGs, we find $f_h = 1.4 \pm 0.4$. These results are consistent with the mean ellipticity of the galaxy light for the lens sample, $e = 0.22$ and the halo ellipticity discussed above, $e = 0.347$. This is a significant detection of a non-zero f_h .

Repeating the analysis for the BOSS LRGs, we obtain a mean

halo ellipticity of $e = 0.170 \pm 0.095$. Using the HM estimators, we obtain $f_h = 0.1 \pm 0.4$. The results for the CJ estimators are shown in Fig. 5, while the results for the HM estimators are displayed in Fig. 6. Taken at face value, these haloes appear to be less elliptical than the DR7 LRG haloes, although the difference in e is not statistically significant. The difference in f_h , however, is significant at the $\sim 2\sigma$ level. The reasons for this are not clear, but there are a number of possibilities. First, the BOSS LRGs are slightly less massive than the SDSS DR7 LRGs, which may cause them to be less elliptical (see discussion in Section 6). Moreover, the BOSS LRG sample is more distant ($z_{\text{median}} = 0.51$) than the SDSS DR7 LRGs ($z_{\text{median}} = 0.34$). At these redshifts there is loss of surface brightness, not only due to cosmological $(1+z)^4$ dimming but also because the CFHT r -band probes the rest-frame ultraviolet below the 4000 Å break, where the flux from old, red galaxies is much suppressed. This may lead to less accurate measurements of the LRG ellipticity and of the major-axis position angle of the galaxy light, leading to greater misalignment when stacking. Also, for the above reasons, photometry may be more sensitive to the inner regions of the BOSS LRGs whereas for the SDSS DR7 LRGs it may be more sensitive to the outer regions. In an elliptical galaxy with isophote twists, the latter may be better aligned with the DM halo. Finally, [Schrabback et al. \(2015\)](#), in their fig. 6., have shown that the HM estimators of f_h are biased low due to cosmic shear when the data extend to high galactocentric projected radii for lenses in the redshift range of the BOSS LRGs, whereas this bias is negligible for the lower redshift SDSS DR7 LRGs.

5 SYSTEMATIC TESTS

5.1 Lens major axis position angles from SDSS

When using lens position angles from UNIONS, the shape measurements of the sources and lenses are both derived from the same imaging. It is possible that issues with the shape measurements, for example inadequate PSF correction, could lead to a correlation between the lens and source shapes. This correlation could lead to an observed alignment that could affect our weak lensing results. To provide an alternate test, and an independent source of lens position angles, we can perform the quadrupole shear measurement using position angles from the SDSS database. First, all LRGs were selected from the DR16 release of SDSS using $z_{\text{noqso}} > 0$ and $\text{sourceType} = \text{LRG}$. The resulting list of LRGs were then matched in equatorial coordinates to our list of LRGs that overlap with UNIONS. In SDSS, these LRGs were fit with both an exponential and a de Vaucouleurs profile. The angle from the fit with the highest likelihood was chosen. It is worth noting that the SDSS imaging is considerably shallower than UNIONS, so we might expect their position angles to be less accurate than the position angles from UNIONS. A histogram of the differences in position angle from UNIONS and SDSS is displayed in Fig. 7. Most position angles are similar, however, there is a significant number of LRGs that have substantially different major-axis position angles in SDSS photometry versus UNIONS photometry. The semi-interquartile range of the difference is 31.4° and the standard deviation is 33.6° .

The process of calculating the quadrupole shear was repeated using the major axis light position angles from SDSS. Results for the quadrupole shear using the SDSS lens position angle are displayed in Fig. 8. We can repeat the process used for the UNIONS major axis position angles and calculate the mean halo ellipticity and χ^2 of the fit. The mean halo ellipticity is $e = 0.250 \pm 0.091$ and $\chi^2_{\nu} = 0.66$. This is similar to the results obtained by [Clampitt & Jain \(2016\)](#),

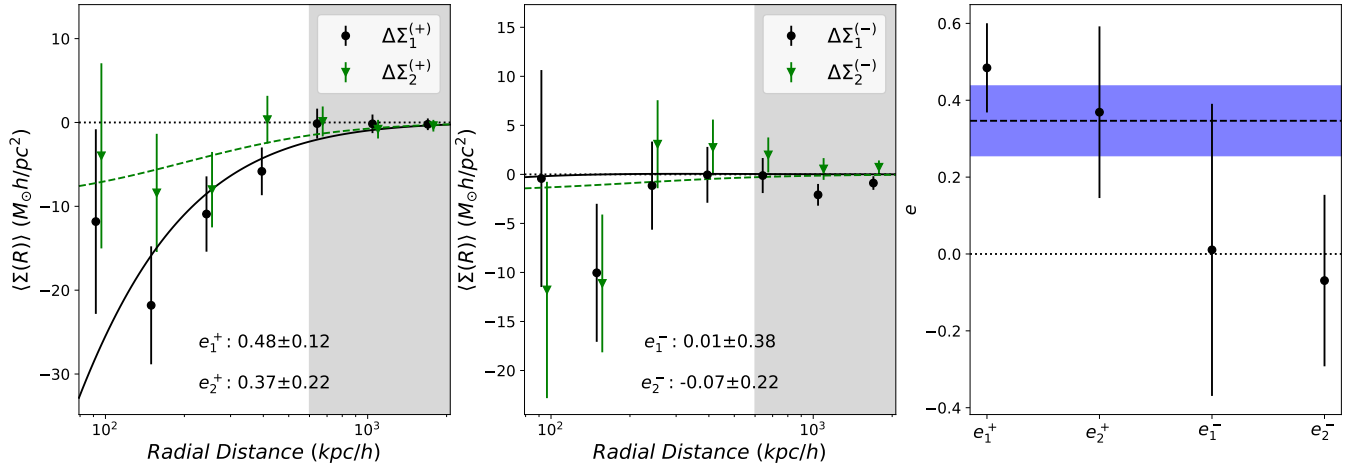


Figure 3. Quadrupole shear around LRGs aligned with the major axis of the LRG light. Results obtained after correcting for systematics are shown. The left subplot displays the positive CJ estimators, while the centre subplot displays the negative CJ estimators. The first estimator is represented in black with circles and a solid line. The second estimator is represented in green with triangles and a dashed line. Points plotted in green have been shifted slightly to the right for clarity. The best fit of e for each estimator is displayed in each subplot. The right subplot displays the halo ellipticity values from the 4 independent CJ estimators. The weighted average halo ellipticity ($e = 0.347$) is plotted as a dashed black line. The range of 1σ uncertainty in the mean is shaded in blue ($\Delta e = 0.091$). No ellipticity is represented with a dotted black line at $e = 0$.

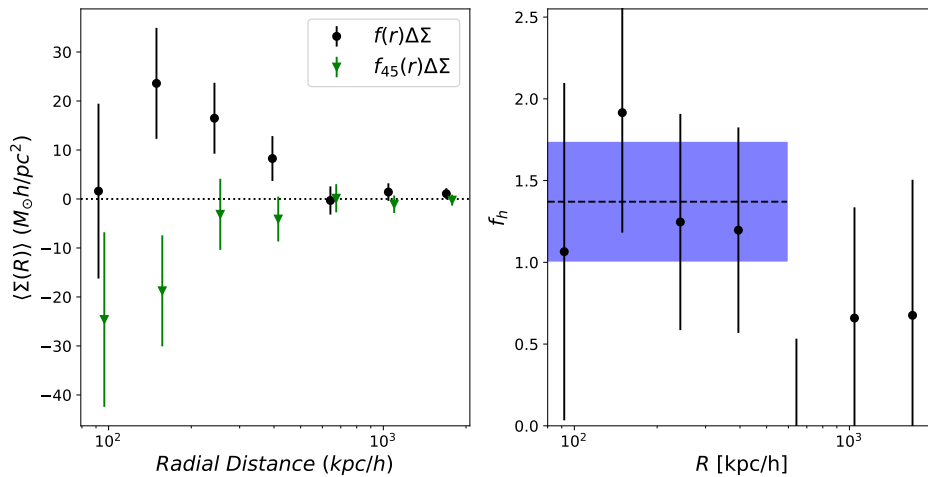


Figure 4. The left subplot displays the HM estimators. This subplot is formatted in the same way as the left and centre subplots from Fig. 3. The right subplot displays each measurement of $f_h(r) = \hat{\gamma}(r) / \hat{\kappa}(r)$. The weighted mean value within the virial radius, $f_h = 1.4 \pm 0.4$, is displayed as a black dashed line, while the uncertainty is shaded in blue. The black dashed line and shaded region are only plotted up to the virial radius.

$e = 0.24 \pm 0.06$, who used SDSS photometry to study the same set of LRGs. The mean ellipticity from the SDSS position angles is lower than for the UNIONS position angles. This is not surprising: as mentioned before, the imaging from SDSS is shallower than it is for UNIONS, so we expect the position angles to be less accurate. This could lead to a higher degree of misalignment which would yield a rounder stacked shear.

To assess this effect, we note that the misalignment between the UNIONS major axis and the SDSS major axis will obey some probability distribution, $P(\theta_{\text{mis}})$, which describes how likely the two axes will be separated by a given misalignment angle, as shown in Fig. 7. In Sec. 3.2.3 we discussed the effect of a misalignment between the stellar light and the DM halo. However, observational errors due to signal-to-noise when measuring the major axis of the stellar light will also contribute to the misalignment. Moreover, differences may also arise because elliptical galaxies have isophote twists, and so deeper

photometry may probe outer regions of the galaxies which may have an different ellipticity and position angle than the inner regions.

If the SDSS light angles are misaligned, they will yield a lower e_{eff} than the ellipticity we measure from the UNIONS light angles, e , as given by equation (35). In Fig. 7, we found a standard deviation between the UNIONS and SDSS angles of $\sigma = 33.6^\circ$. If we attribute all of the misalignment in the lens positions to errors in the SDSS photometry, using the standard deviation from Fig. 7, we should obtain an effective ellipticity of $e_{\text{eff}} = 0.175$ for SDSS. This is somewhat lower than the observed value. In reality, there will be some measurement uncertainty in both the UNIONS and SDSS major axis position angles, although we expect the latter to be larger due to the shallower depth of the photometry.

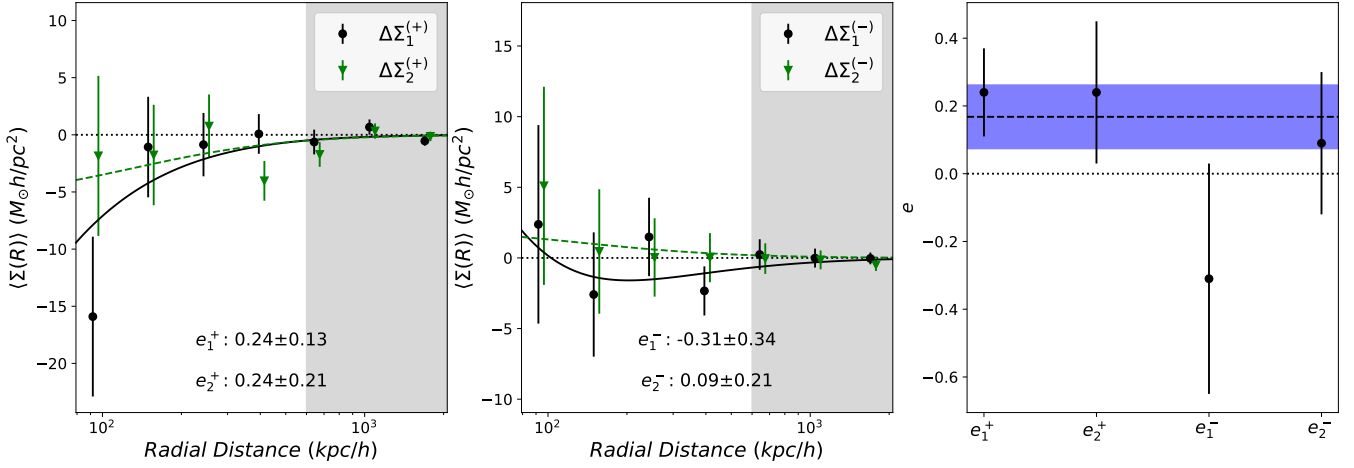


Figure 5. Results for the CJ estimators and halo ellipticity presented in the same format as Fig. 3. The lens sample is composed of 144,000 from the CMASS and LOWZ samples of BOSS.

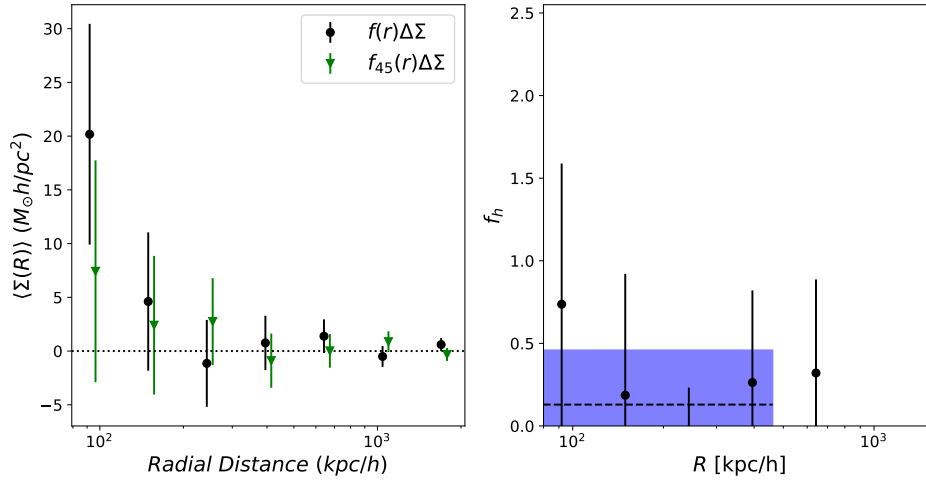


Figure 6. Results for the HM estimators and f_h calculated using the the CMASS and LOWZ samples of BOSS. In the right subplot, $f_h = 0.1 \pm 0.4$. Results are presented in the same format as Fig. 4.

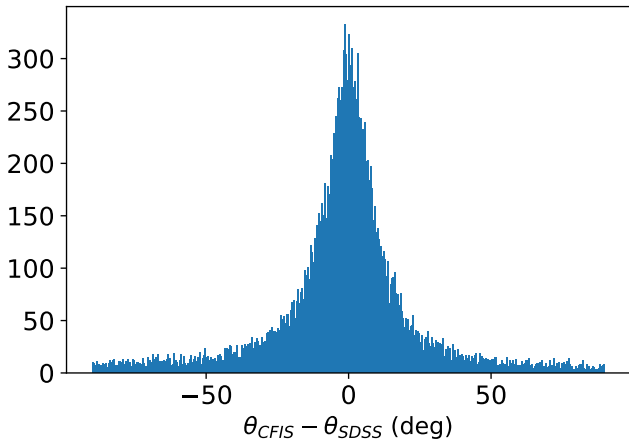


Figure 7. Comparison of the position angles of the major axis of light in lens galaxies measured in UNIONS and in SDSS.

5.2 Satellite Galaxies

There is no redshift information for sources from UNIONS yet. As a result, we have no way of knowing which sources are actually behind the lens and therefore which are affected by weak lensing. Some portion of the sources surrounding the lenses are actually satellite galaxies. These satellite galaxies are not affected by lensing, and may introduce bias in the form of coherent intrinsic alignment. In this section, we will address this concern and attempt to quantify the effect of satellite galaxies on our measurement of halo ellipticity.

Previously, we discussed the azimuthal distribution of sources around the lenses. Specifically, that an excess of sources along the lens major axis and a deficit along the minor axis suggests a portion of the source sample are actually satellite galaxies. This alignment between the satellite distribution and the alignment of the central galaxy has been observed by Yang et al. (2006), who observed a stronger alignment for red central galaxies. Our lenses, being LRGs, are therefore expected to be significantly aligned with their satellite populations. The amplitude of this non-uniform source distribution was $3.6 \pm 0.3\%$.

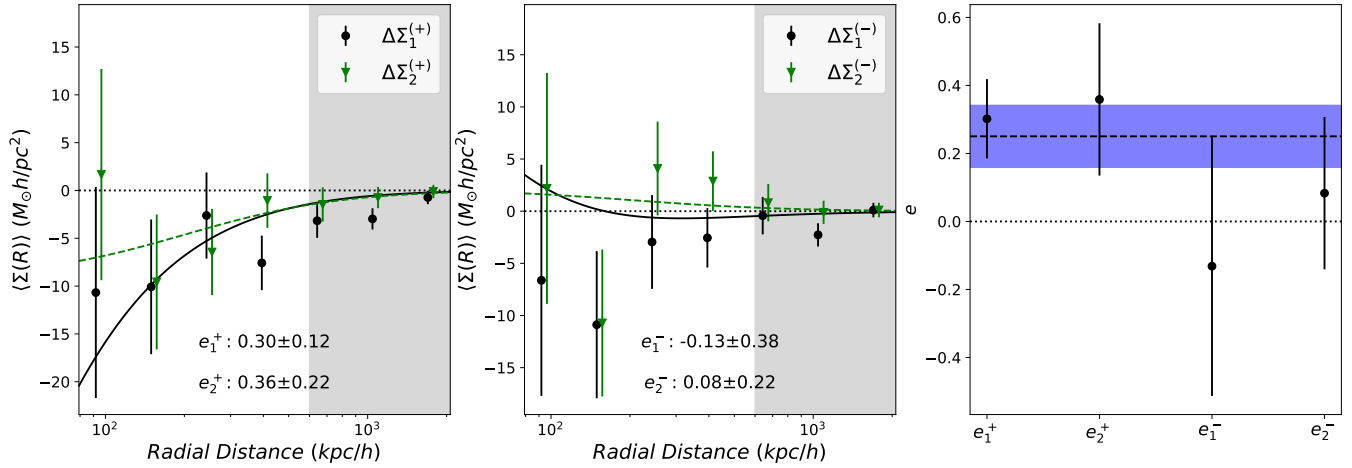


Figure 8. Results for the CJ estimators and halo ellipticity presented in the same format as Fig. 3. The lens position angle from SDSS was used, as opposed to the lens position angle from UNIONS.

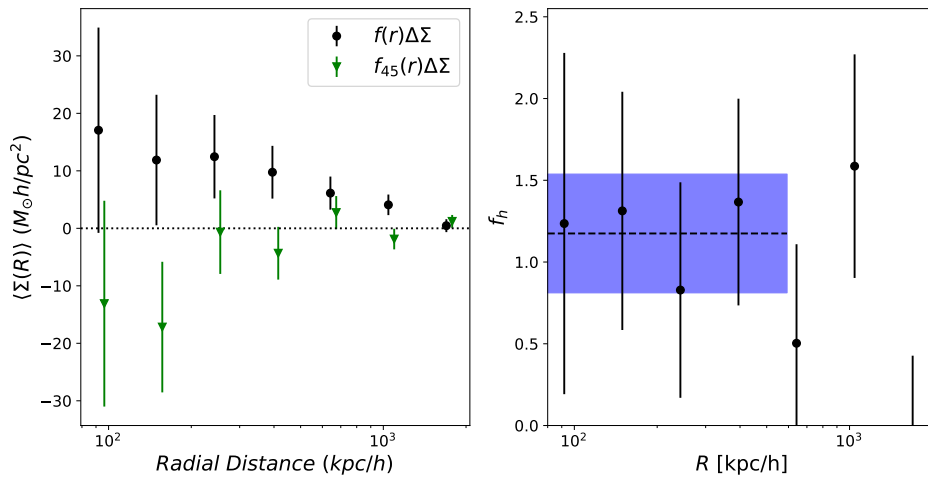


Figure 9. Results for the HM estimators and f_h calculated using the SDSS light angles. In the right subplot, $f_h = 1.2 \pm 0.4$. Results are presented in the same format as Fig. 4.

Light from the lens will contaminate the shape measurements of the plentiful sources along the lens major axis. This can lead to the shape measurement being biased in the radial direction (Sifón et al. 2018). In addition to this source of contamination, there is also contamination due to intrinsic alignment of the satellite galaxies. Schneider & Bridle (2010) propose a model for intrinsic alignments of galaxies. Their model is based on the linear alignment model, which assumes the alignment of galaxies is linearly proportional to the tidal field. This model predicts preferential radial alignment of satellites with the central galaxy. However, observational studies have found mixed results. Several studies of satellite alignment yield results consistent with random alignment (Sifón et al. 2015; Schneider et al. 2013), although preferential radial alignment has been observed in others (Singh et al. 2015; Georgiou et al. 2019). If there is a significant preferential radial alignment, an excess of satellites along the major axis will lead to a larger negative contribution near the major axis. This will have the effect of adding a negative quadrupole term, or a negative halo ellipticity, to our results.

We can attempt to quantify how much of an effect we could expect these satellite galaxies to have on our measured halo ellipticity. When

aligning with UNIONS angles, approximately 3.6% of sources follow a $\cos(2\theta)$ distribution. Presumably the amount of sources that are satellites is actually much higher. However, most of them will bias the monopole. Only the portion that are distributed with $\cos(2\theta)$ dependence will negatively bias our ellipticity.

Georgiou et al. (2019) observed a radial dependence for the amount of contamination due to satellite galaxies, although this effect is only significant within $\sim 0.3R_{200c}$ from the centre of the lens. From the mean halo mass of the lens sample, we can calculate the average virial radius and determine which radial bins may be susceptible to contamination. Sources close to the centre will experience a significant amount of contamination. However, sources within 70 kpc/h of the lens are not included in the weighted average. Sources within the innermost two radial bins will experience a mean radial shear of $\langle e_+ \rangle \sim 0.005$ (Georgiou et al. 2019), according to their distance compared to the average virial radius of these lenses. This is more significant than the effect in reality, but we have increased the effect in order to be as conservative as possible with this estimate.

We can examine how susceptible our measurements of halo ellipticity are to this radial bias. We assume satellites in the two innermost

radial bins of the quadrupole estimator will experience a radial bias of $\langle e_+ \rangle = 0.005$. In order to calculate how this will affect the mass density we can use $\Delta\Sigma(r) = \Sigma_{\text{crit}}\gamma(r)$. Our lenses will each have a different Σ_{crit} depending on their redshift, but we can calculate the critical density for each lens to determine the average value. As we saw in Fig. 1, 3.6% of our sources contribute a radial quadrupole shear. When combined with the average critical density, this will lead to a change in the mass density of at most $\Delta\Sigma = 1.08M_{\odot}h \text{ pc}^2$ in the two innermost bins. There will be no significant change in the mass density in any of the other bins.

If we change the two innermost bins of each quadrupole estimator by $1.08M_{\odot}h \text{ pc}^2$, we can estimate how susceptible the mean halo ellipticity is to this negative quadrupole effect. The negative quadrupole effect will manifest as excess radial shear along the major axis of the lens and excess tangential shear along the minor axis. This will affect each of the estimators in a different way. Examining how the mean halo ellipticity changes, if all estimators are affected, will give us a conservative estimate of how sensitive our results are to contamination from satellite galaxies.

Fig. 10 displays results after applying a bias due to satellite galaxies. The positive CJ estimators are displayed in the left and centre subplots. The two innermost bins has been changed by $\pm 1.08M_{\odot}h \text{ pc}^2$ and the fit has been repeated. The right subplot displays the results of calculating the mean halo ellipticity using the CJ estimators. The format is the same as previous mean ellipticity plots, but a red band has been added to represent how much the mean ellipticity changes due to contamination from satellite galaxies. This effect yields an upper limit of $e = 0.366$ and a lower limit of $e = 0.326$ compared to our mean halo ellipticity of $e = 0.346 \pm 0.091$. Even a conservative estimate of the effects of contamination from satellite galaxies yields results well within the 1σ range of uncertainty of the mean halo ellipticity. This suggests contamination from satellite galaxies does not have a significant effect on our results.

6 DISCUSSION

In order to measure the ellipticity of the dark matter halo, we studied the quadrupole shear. The 4 CJ estimators provide independent measurements of the halo ellipticity, and taking a weighted average of these 4 estimators will yield a mean halo ellipticity. The mean halo ellipticity of the lens sample was measured to be $e = 0.35 \pm 0.09$.

Our results are in good agreement with other results from weak lensing. In particular, Clampitt & Jain (2016) studied the halo ellipticity of the same DR7 LRGs as in this paper using the same CJ estimators. Their best fit is a halo ellipticity of $e = 0.24 \pm 0.06$. This is similar to our result of $e = 0.25 \pm 0.09$ from Sec. 5 where, like them, we used SDSS photometry for the major axis of the light.

Fig. 11 compares our results for the constraints on e with those from the literature that are based on aligning the weak lensing with the major axis of red galaxies. Studies included are: the red lens galaxies from Georgiou et al. (2021) and Schrabback et al. (2021); the group-centrals from Van Uitert et al. (2017), where we use their fit over the range of 28 – 525 kpc/h, which is similar to our fitted range; the study of DR7 LRGs by Clampitt & Jain (2016), and the cluster study of Shin et al. (2018), where we use their result for alignment between the BCG and the cluster halo. We have converted results to use our conventions for ellipticity, e , and mass, M_{200c} . Horizontal error bars represent approximate lens mass ranges for each study.

To test whether the apparent trend of increasing ellipticity with halo mass is statistically significant, we fit a straight line to e as a function of M_{200c} using the data plotted in Fig. 11. The resulting fit

is

$$e = (0.20 \pm 0.03) + (0.10 \pm 0.05) \log_{10} \left(\frac{M_{200c}}{10^{13}M_{\odot}/h} \right). \quad (36)$$

This then suggests that the increase in ellipticity with halo mass is statistically significant at approximately the 2σ confidence level.

The trend above is in agreement with N-body simulations which predict that haloes are more prolate with increasing mass. Fig. 12 shows the predicted ellipticity, e , for triaxial DM haloes with axis ratios 1:q:s, as a function of q and s , after projecting to 2D using Ryden (1992) then averaging over random projection angles. Expected DM halo shapes from Tenneti et al. (2014) for $M_{200c} = 10^{12}, 10^{13}, 10^{14}, 10^{15} h^{-1}M_{\odot}$ at $z = 0.34$ (same as DR7 LRGs) are shown in Fig. 12 and overplotted in Fig. 11. These predict a slope of 0.06 per decade in mass, flatter than the value in equation (36).

As discussed in Sec. 3.2.3, we do not expect the major axis of the stellar light to be perfectly aligned with the major axis of the projected DM halo. This leads to a lower “effective” ellipticity, e_{eff} , measured by weak lensing. We consider two models for misalignment, both based on hydrodynamical simulations. Tenneti et al. (2014) found low misalignment, leading to high e_{eff}/e ratios of 0.68 and 0.96 at $M_{200c} = 10^{12}$ and $3 \times 10^{13} h^{-1}M_{\odot}$, respectively. On the other hand, the typical misalignment measured by Velliscig et al. (2015) is larger, leading to lower values of e_{eff}/e than Tenneti et al. (2014) (see Appendix A). Both are shown in Fig. 11. In both cases the alignment increases with increasing halo mass, leading to a steeper slope of e_{eff} with halo mass, in better agreement with the observations. Overall, the Tenneti et al. (2014) predictions are slightly but not significantly higher than the observational trend over the mass range covered by that study, while the Velliscig et al. (2015) predictions are, on average, lower than the observational fit. However, there are two important caveats regarding these comparisons. First, here we focus on red galaxies, whereas the results quoted above for simulations do not distinguish between red and blue galaxies. Second, Velliscig et al. (2015) uses the major axis of stars within the stellar half-mass radius. Our major and minor axes are based on second moments above an isophotal threshold (Bertin & Arnouts 1996, SExtractor). The position angles determined this way may be based on light that is more extended than those determined within the half-mass radius. Velliscig et al. (2015) show that the alignment improves when using stars at larger radii, so it is possible that if they had used a larger radius, the alignment would have been better and the ratio e_{eff}/e higher, bringing their predictions into better agreement. It is clear that future observational and theoretical studies will need to pay greater attention to measuring major axes and ellipticities in a more consistent way.

7 CONCLUSIONS

We studied the anisotropic lensing signal around LRGs from SDSS with source galaxies from an early internal shape measurement catalogue from UNIONS covering 1,500 square degrees. Fitting an NFW profile to the monopole shear profile of 18,000 DR7 LRGs yields an average mass of $M_{200c} \sim 2.5 \times 10^{13} M_{\odot}/h$. When aligning our coordinate system with the major axis of the lens galaxy stellar light, we measure a mean halo ellipticity of $e = 0.35 \pm 0.09$ and an aligned ellipticity ratio of $f_h = 1.4 \pm 0.4$. This value is in agreement with other measurements of halo ellipticity from weak lensing (Clampitt & Jain 2016; Van Uitert et al. 2017). The 144,000 LRGs from BOSS are less massive, with an average mass of $M_{200c} = 1.1 \times 10^{13} M_{\odot}/h$.

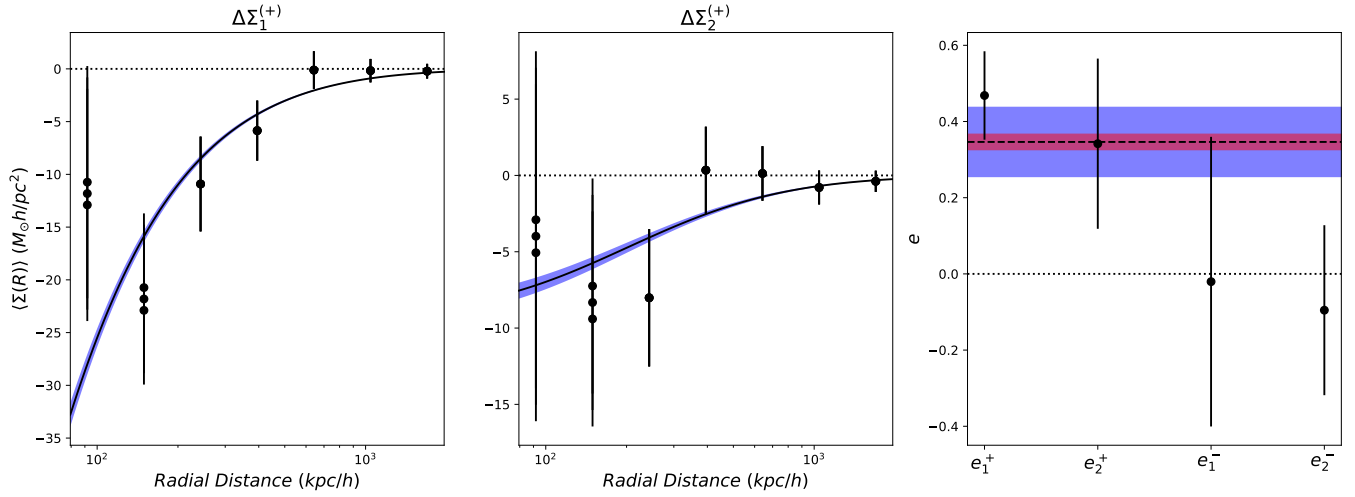


Figure 10. Results for quadrupole shear after applying bias due to satellite galaxies. Positive CJ estimators are displayed in the left and centre subplots. The two innermost bins has been changed by $\pm 1.08 M_\odot h \text{pc}^2$ and the fit has been repeated. The shaded blue area represents how much the fit can vary as the inner bins are shifted. On the right are the results of calculating mean ellipticity using the CJ estimators. A red band has been added to represent how much the mean ellipticity changes due to contamination from satellite galaxies.

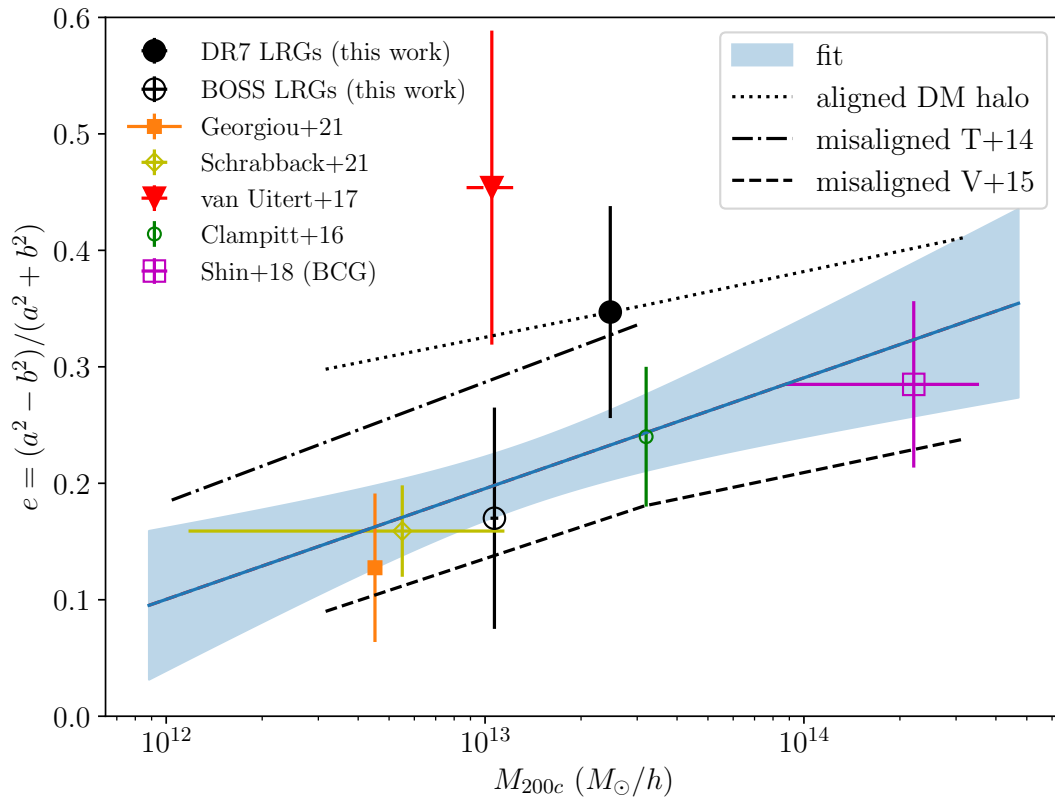


Figure 11. Comparison of constraints on halo ellipticity e as a function of halo mass for red galaxies, groups, and clusters. Where present, horizontal error bars represent approximate lens mass ranges for each study. We show the results from this paper and the papers cited in the text. The blue shaded band shows the fit to all data points, as described in the text. The dotted line indicates the expected trend from N-body simulations assuming DM halos are perfectly aligned with the stellar light whereas the dot-dash and dashed lines show the predictions using the misalignment models of [Tenneti et al. \(2014\)](#) and [Velliscig et al. \(2015\)](#), respectively.

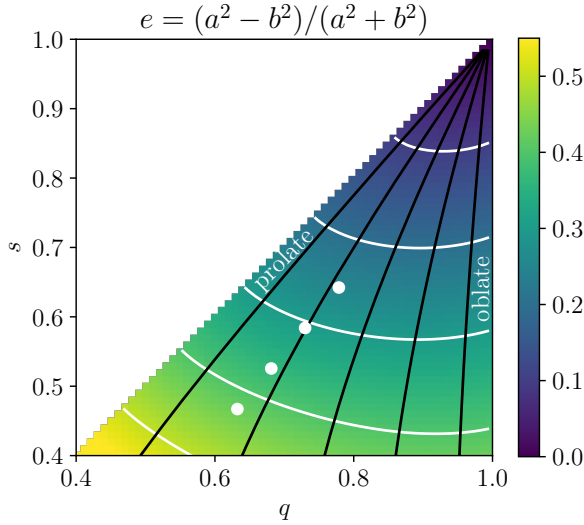


Figure 12. The projected 2D ellipticity, e , for triaxial DM halos with axis ratios $1:q:s$, as a function of q and s , averaged over random projection angles is shown by the colour bar and the white contours (steps of 0.1). Round halos are at the top right corner, prolate halos along the diagonal axis and oblate halos along the right hand axis. Black lines are constant triaxiality $T = (1 - q^2)/(1 - s^2) = 0.1, 0.3, 0.5, 0.7, 0.9$, respectively from right (oblate) to left (prolate). The expected DM halo shapes from Tenneti et al. (2014) for $M_{200c} = 10^{12}, 10^{13}, 10^{14}, 10^{15} h^{-1} M_{\odot}$ at $z = 0.34$ are shown respectively from top right to lower left by white circles.

Repeating the analysis for the LRGs from BOSS, we found a mean halo ellipticity of $e = 0.17 \pm 0.1$ and an aligned ellipticity ratio of $f_h = 0.1 \pm 0.4$.

Combining our results together with previous measurements of halo ellipticity yields a trend with ellipticity increasing 0.10 ± 0.05 per decade in halo mass.

The prospects for improving halo ellipticity measurements from weak lensing are very promising. UNIONS is still underway, with the goal of covering 4, 800 square degrees with high quality multi-band imaging, which will yield photometric redshifts for source galaxies. The UNIONS survey area has large overlap with the footprint of the SDSS-based spectroscopic surveys, and, in the near future, the Dark Energy Spectroscopic Instrument (DESI Collaboration et al. 2016), which will allow larger and more comprehensive lens catalogues.

ACKNOWLEDGEMENTS

We thank the referee for useful comments that improved this paper.

MJH acknowledges funding from an NSERC Discovery Grant. HH is supported by a DFG Heisenberg grant (Hi 1495/5-1), the DFG Collaborative Research Center SFB1491, as well as an ERC Consolidator Grant (No. 770935).

This work is based on data obtained as part of the Canada-France Imaging Survey, a CFHT large program of the National Research Council of Canada and the French Centre National de la Recherche Scientifique. This work is additionally based on observations obtained with MegaPrime/MegaCam, a joint project of CFHT and CEA Saclay, at the Canada-France-Hawaii Telescope (CFHT) which is op-

erated by the National Research Council (NRC) of Canada, the Institut National des Science de l'Univers (INSU) of the Centre National de la Recherche Scientifique (CNRS) of France, and the University of Hawaii. We are honored and grateful for the opportunity of observing the Universe from Maunakea, which has the cultural, historical and natural significance in Hawaii. This research used the facilities of the Canadian Astronomy Data Centre operated by the National Research Council of Canada with the support of the Canadian Space Agency.

DATA AVAILABILITY

A subset of the raw data underlying this article are publicly available via the Canadian Astronomical Data Center at <http://www.cadc-ccda.hia-ihp.nrc-cnrc.gc.ca/en/megapipe/>. The remaining raw data and all processed data are available to members of the Canadian and French communities via reasonable requests to the principal investigators of the Canada-France Imaging Survey, Alan McConnachie and Jean-Charles Cuillandre. All data will be publicly available to the international community at the end of the proprietary period, scheduled for 2023.

REFERENCES

- Adhikari S., Chue C. Y. R., Dalal N., 2015, *J. Cosmology Astropart. Phys.*, **2015**, 009
- Allgood B., Flores R. A., Primack J. R., Kravtsov A. V., Wechsler R. H., Faltenbacher A., Bullock J. S., 2006, *MNRAS*, **367**, 1781
- Azzaro M., Patiri S. G., Prada F., Zentner A. R., 2007, *MNRAS*, **376**, L43
- Bailin J., Steinmetz M., 2005, *ApJ*, **627**, 647
- Baltz E. A., Marshall P., Oguri M., 2009, *J. Cosmology Astropart. Phys.*, **1**, 015
- Bertin E., Arnouts S., 1996, *A&AS*, **117**, 393
- Brainerd T. G., 2005, *ApJ*, **628**, L101
- Brainerd T. G., Wright C. O., 2000, arXiv e-prints, pp astro-ph/0006281
- Clampitt J., Jain B., 2016, *MNRAS*, **457**, 4135
- DESI Collaboration et al., 2016, arXiv e-prints, p. arXiv:1611.00036
- Davé R., Spergel D. N., Steinhardt P. J., Wandelt B. D., 2001, *ApJ*, **547**, 574
- Dawson K. S., et al., 2013, *AJ*, **145**, 10
- Dubinski J., Carlberg R. G., 1991, *ApJ*, **378**, 496
- Duffy A. R., Schaye J., Kay S. T., Dalla Vecchia C., 2008, *MNRAS*, **390**, L64
- Dutton A. A., Macciò A. V., 2014, *MNRAS*, **441**, 3359
- Erben T., et al., 2013, *MNRAS*, **433**, 2545
- Evans A. K. D., Bridle S., 2009, *ApJ*, **695**, 1446
- Georgiou C., et al., 2019, *A&A*, **628**, A31
- Georgiou C., et al., 2021, *A&A*, **647**, A185
- Guinot A., et al., 2022, arXiv e-prints, p. arXiv:2204.04798
- Hildebrandt H., et al., 2012, *MNRAS*, **421**, 2355
- Hildebrandt H., et al., 2017, *MNRAS*, **465**, 1454
- Hildebrandt H., et al., 2020, *A&A*, **633**, A69
- Hoekstra H., Yee H. K. C., Gladders M. D., 2004, *ApJ*, **606**, 67
- Huff E., Mandelbaum R., 2017, arXiv e-prints, p. arXiv:1702.02600
- Ibata R. A., et al., 2017, *ApJ*, **848**, 128
- Jing Y. P., Suto Y., 2002, *ApJ*, **574**, 538
- Kazin E. A., et al., 2010, *ApJ*, **710**, 1444
- Khoury J., 2015, *Phys. Rev. D*, **91**, 024022
- Libeskind N. I., Cole S., Frenk C. S., Okamoto T., Jenkins A., 2007, *MNRAS*, **374**, 16
- Lima M., Cunha C. E., Oyaizu H., Frieman J., Lin H., Sheldon E. S., 2008, *MNRAS*, **390**, 118
- Mandelbaum R., Hirata C. M., Broderick T., Seljak U., Brinkmann J., 2006a, *MNRAS*, **370**, 1008
- Mandelbaum R., Seljak U., Cool R. J., Blanton M., Hirata C. M., Brinkmann J., 2006b, *MNRAS*, **372**, 758
- Milgrom M., 2013, *Phys. Rev. Lett.*, **111**, 041105

Natarajan P., Refregier A., 2000, *ApJ*, **538**, L113
 Oguri M., Takada M., Okabe N., Smith G. P., 2010, *MNRAS*, **405**, 2215
 Parejko J. K., et al., 2013, *Monthly Notices of the Royal Astronomical Society*, **429**, 98
 Parker L. C., Hoekstra H., Hudson M. J., van Waerbeke L., Mellier Y., 2007, *ApJ*, **669**, 21
 Peter A. H. G., Rocha M., Bullock J. S., Kaplinghat M., 2013, *MNRAS*, **430**, 105
 Ryden B., 1992, *The Astrophysical Journal*, **396**, 445
 Schneider M. D., Bridle S., 2010, *MNRAS*, **402**, 2127
 Schneider M. D., et al., 2013, *MNRAS*, **433**, 2727
 Schrabback T., et al., 2015, *MNRAS*, **454**, 1432
 Schrabback T., et al., 2021, *A&A*, **646**, A73
 Sheldon E., 2015, NGMIX: Gaussian mixture models for 2D images (ascl:1508.008)
 Sheldon E. S., et al., 2004, *AJ*, **127**, 2544
 Shin T.-h., Clampitt J., Jain B., Bernstein G., Neil A., Rozo E., Rykoff E., 2018, *MNRAS*, **475**, 2421
 Sifón C., Hoekstra H., Cacciato M., Viola M., Köhlinger F., van der Burg R. F. J., Sand D. J., Graham M. L., 2015, *A&A*, **575**, A48
 Sifón C., Herbonnet R., Hoekstra H., van der Burg R. F. J., Viola M., 2018, *MNRAS*, **478**, 1244
 Singh S., Mandelbaum R., More S., 2015, *MNRAS*, **450**, 2195
 Tenneti A., Mandelbaum R., Di Matteo T., Feng Y., Khandai N., 2014, *MNRAS*, **441**, 470
 van Haarlem M., van de Weygaert R., 1993, *ApJ*, **418**, 544
 van Uitert E., et al., 2017, *MNRAS*, **467**, 4131
 Velliscig M., et al., 2015, *MNRAS*, **453**, 721
 Viola M., et al., 2015, *MNRAS*, **452**, 3529
 White M., et al., 2011, *The Astrophysical Journal*, **728**, 126
 Yang X., van den Bosch F. C., Mo H. J., Mao S., Kang X., Weinmann S. M., Guo Y., Jing Y. P., 2006, *MNRAS*, **369**, 1293
 Zentner A. R., Kravtsov A. V., Gnedin O. Y., Klypin A. A., 2005, *ApJ*, **629**, 219
 Zheng Z., Zehavi I., Eisenstein D. J., Weinberg D. H., Jing Y. P., 2009a, *ApJ*, **707**, 554
 Zheng Z., Zehavi I., Eisenstein D. J., Weinberg D. H., Jing Y. P., 2009b, *The Astrophysical Journal*, **707**, 554

APPENDIX A: MISALIGNMENTS IN VELLISCIG ET AL. 2015

Velliscig et al. (2015) propose that the misalignment, θ_{mis} between the projected major axis of the stellar light and that of the DM halo has a probability density that takes the form of the double Gaussian,

$$P(\theta_{\text{mis}}) = C \exp\left(-\frac{\theta_{\text{mis}}^2}{2\sigma_1^2}\right) + D \exp\left(-\frac{\theta_{\text{mis}}^2}{2\sigma_2^2}\right) + E. \quad (\text{A1})$$

They tabulate parameters of the fit in their table B2. There is, however, a typographical error in that table. Consequently, we digitised their fig. 10 and refitted the parameters using the same functional form: the results are given in Table A1. The LRG lenses studied in this paper are best described by the $13 < \log_{10}(M_{200c}/[M_{\odot}h^{-1}]) < 14$ halo mass bin.

This paper has been typeset from a $\text{\TeX}/\text{\LaTeX}$ file prepared by the author.

Table A1. Fit parameters for equation (A1) that describes the probability density function of the misalignment between the projected stellar distribution and the projected total matter distribution, based on fig. 10 from Velliscig et al. (2015). The mass bin column gives the range in units $\log_{10}[M_{200c}/(h^{-1}M_{\odot})]$. θ_{mean} and θ_{med} are the mean and median misalignment angles, respectively. The probability density function is normalized to unity over the range 0° to 90° .

mass bin	σ_1 deg	σ_2 deg	C deg $^{-1}$	D deg $^{-1}$	E deg $^{-1}$	θ_{mean} deg	θ_{med} deg	e_{eff}/e
11 – 12	5.1	28.3	0.0273	0.0085	0.0058	30	24	0.36
12 – 13	5.1	31.6	0.0070	0.0118	0.0054	33	28	0.30
13 – 14	14.8	32.9	0.0200	0.0086	0.0030	25	18	0.51
14 – 15	9.6	25.9	0.0239	0.0142	0.0028	22	15	0.58